Photoacoustics 38 (2024) 100620

Contents lists available at ScienceDirect

Photoacoustics

journal homepage: www.elsevier.com/locate/pacs

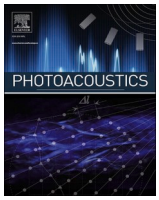

Wavelength-modulated photoacoustic spectroscopic instrumentation system for multiple greenhouse gas detection and in-field application in the Qinling mountainous region of China

Lixian Liu [a,b], Huiting Huan [a,c,*], Xueshi Zhang [a], Le Zhang [a], Jinsong Zhan [a,c], Shaowei Jiang [d], Xukun Yin [a], Baisong Chen [a,**], Xiaopeng Shao [a], Xuesen Xu [e], Andreas Mandelis [a,b,*]

[a] School of Optoelectronic Engineering, Xidian University, Xi'an 710071, China
[b] Center for Advanced Diffusion-Wave and Photoacoustic Technologies (CADIPT), Department of Mechanical and Industrial Engineering, and Institute for Advanced Non-Destructive and Non-Invasive Diagnostic Technologies (IANDIT), University of Toronto, Toronto M5S 3G8, Canada
[c] State Key Laboratory of Electromechanical Integrated Manufacturing of High-performance Electronic Equipments, Xidian University, Xi'an 710071, China
[d] School of Communication Engineering, Hangzhou Dianzi University, Hangzhou 310018, China
[e] School of Physics and Optoelectronic Engineering, Hangzhou Institute for Advanced Study, University of Chinese Academy of Sciences, Hangzhou 310024, China

ARTICLE INFO

Keywords:
Multiple gas monitoring
Greenhouse
In-situ detection
Photoacoustic spectroscopy

ABSTRACT

We present a sensitive and compact quantum cascade laser-based photoacoustic greenhouse gas sensor for the detection of CO_2, CH_4 and CO and discuss its applicability toward on-line real-time trace greenhouse gas analysis. Differential photoacoustic resonators with different dimensions were used and optimized to balance sensitivity with signal saturation. The effects of ambient parameters, gas flow rate, pressure and humidity on the photoacoustic signal and the spectral cross-interference were investigated. Thanks to the combined operation of in-house designed laser control and lock-in amplifier, the gas detection sensitivities achieved were 5.6 ppb for CH_4, 0.8 ppb for CO and 17.2 ppb for CO_2, signal averaging time 1 s and an excellent dynamic range beyond 6 orders of magnitude. A continuous outdoor five-day test was performed in an observation station in China's Qinling National Botanical Garden (E longitude 108°29', N latitude 33°43') which demonstrated the stability and reliability of the greenhouse gas sensor.

1. Introduction

Reducing emissions from the extraction, transportation and burning of fossils fuels is an important mechanism for many countries in order to limit their greenhouse gas emissions by 2030 and thereby reduce the impact of climate change [1]. Verification of reduction in emissions, especially of the latent type, will become increasingly important in assessing the effectiveness of low emission technologies and greenhouse gas reduction strategies. Atmospheric monitoring technologies are an ideal method for investigating latent emissions of greenhouse gases and quantifications of leakage events [2]. High confidence in the accuracy of the quantification methods employed is therefore essential and is a legislative requirement of various governments [3]. CO_2 and CH_4 are the two most important greenhouse gases, reflecting infrared radiation, thus some of the heat leaving the Earth bounces off the greenhouse gases in the atmosphere and comes back to the Earth's surface[4]. CO is identified as an important indirect greenhouse gas. Model calculations indicate that the emission of 100 Mt (10^{12} g) of CO stimulates an atmospheric chemistry perturbation that is equivalent to direct emission of about 5 Mt of CH_4[4].

There have been a number of recent attempts using optical detection methods to improve atmospheric techniques for quantifying greenhouse gas emissions, which can be applied for the monitoring of urban atmospheric greenhouse gases and marine carbon sinks. Identification of source gas location was accomplished by the atmospheric tomography technique [5]. However, it was less successful with CO_2 emissions due to the lower signal-to-noise ratio (SNR). A good example for Tunable Diode Laser Absorption Spectroscopy (TDLAS) was reported as an instrument consisting of two gallium antimonide-based interband cascade lasers and a compact multipass gas cell [6] with methane and ethane

* Corresponding authors at: School of Optoelectronic Engineering, Xidian University, Xi'an 710071, China.
** Corresponding author.
E-mail addresses: hthuan@xidian.edu.cn (H. Huan), chenbaisong@xidian.edu.cn (B. Chen), mandelis@mie.utoronto.ca (A. Mandelis).

https://doi.org/10.1016/j.pacs.2024.100620
Received 28 March 2024; Received in revised form 3 May 2024; Accepted 10 May 2024
Available online 13 May 2024

sensitivities 5 and 8 ppbv, respectively. Several variations of Optical-Feedback Cavity Ring-Down Spectroscopy (CRDS) have also been used to detect greenhouse gases with ppb level sensitivity [7,8]. Photoacoustic spectroscopy is recognized for its high sensitivity and spectral selectivity [9–15].

Several photoacoustic systems addressing the detection of greenhouse gases have been reported with limits down to 65 pptv for CH_4 [10], 10 ppb for carbon dioxide and 1.5 ppb for CO [16]. However, most of those reports used expensive high-power lasers or bulky laboratory systems and detection was performed under laboratory measurement conditions [17–21].

In the present work, a compact and sensitive greenhouse gas PAS sensor was designed combined with three quantum cascade lasers (QCLs) and an in-house designed field programmable gate array (FPGA) based processing unit. The performance of the sensor was investigated for the detection of greenhouse gases CH_4, CO and CO_2 targeting absorption peaks at 1306.12 cm^{-1}, 2172.76 cm^{-1} and 2345.98 cm^{-1} respectively. This sensor prototype was field tested continuously at China's Qinling National Botanical Garden (E longitude 108°29', N latitude 33°43') for five days and its reliability and feasibility for *in-situ* greenhouse gas monitoring was demonstrated.

2. Photoacoustic sensor design

2.1. PAS system

The configuration of the designed wavelength-modulated (WM) PAS sensor is depicted in Fig. 1. The black, blue and red lines represent the circuit connections, the gas flow direction and the incident laser beam, respectively. The PAS sensor is divided into three parts: Control and Collection Unit (CCU), Photoacoustic Unit (PAU) and Gas Processing Unit (GPU).

With FPGA chip-based (Type EP4CE15F256, Altera®, US) in-house-designed electronics, the CCU has achieved control of the QCLs (customized from Ningbo Healthy Photon Technology Co., LTD, China), lock-in demodulation of photoacoustic signals and real-time-concentration calculation and reporting. The system mainly consists of two parts: laser controller and lock-in module. The sinusoidal dither and ramp signals generated in the FPGA were used for the modulation of the QCLs. A digital orthogonal vector type lock-in amplifier in the FPGA chip was designed, which, unlike single phase sensitive lock-in detectors, was unaffected from phase variation of the reference signal. The frequency-doubling signal of the sinusoidal dither part was used as reference for the acquisition of the in-phase (IP) photoacoustic signal component. A simultaneous 90-degree phase shifted signal was generated through direct digital synthesis set as the reference for detection of the quadrature photoacoustic signal. The in-phase and quadrature photoacoustic components were summed up and averaged for the removal of high frequency signals, and the cut-off frequency of the low-pass filters was set as $f_s/2\,N$ (f_s: sampling frequency, set as 200 kHz; N: summation accumulation number). The photoacoustic amplitude, V_{PA}, was calculated using $V_{PA} = \sqrt{{I_{PA}}^2 + {Q_{PA}}^2}$, where I_{PA} and Q_{PA} are the in-phase and quadrature photoacoustic components after low-pass filtering. For optimal SNR, the time constant of the lock-in amplifier was continuously adjustable and it was equal to N/f_s.

There were three differential resonators with two different sizes in the PAU for the purpose of three target gas detection simultaneously. The resonator sizes for CH_4 and CO detection were identical, but the resonator used for CO_2 had a much shorter optical path to avoid saturation due to the high CO_2 concentration in the atmosphere. More details of the photoacoustic resonator design and optimization are discussed in Sect. 2.3 and in the Appendix. The modulation frequencies (f_1 and f_2) of the sinusoidal waves were set to half the resonance frequencies of the resonators due to 2 f wavelength modulation. The period of the ramp signal was set as 1 s when the WM-PAS system was optimized.

In order to avoid particle and insect contamination in the outdoor field tests, a copper pagoda filter joint and a 2 μm micro-pore PTFE membrane were used at the inlet of the GPU as the first two filters of ambient air. Due to the relaxation effects of photoacoustic signals for the designated target gases, an electron cold trap and humidifier were introduced to increase humidity or remove moisture. The buffers were placed in front of the resonators to maintain gas mixing well and avoid adverse noise of the humidifier (We used a gas washing bottle as the humidifier in the practice. And the bubble from the bottle generates extra noise). The flow rate was controlled with a needle valve and a diaphragm pump which was connected to the outlets of the resonator and the end of the gas flow tube. A pressure controller (LK2, Allcat Scientific®, USA) was put in front of the resonators to control and maintain the pressure in the resonators. Labview-based software was developed to run the CCU and GPU remotely and perform both laser control and photoacoustic measurements. The CCU could also communicate with external devices through a USB connection, receiving commands and transmitting signal data. All sensitive cable connections were designed as coaxial cables with grounded shielding to prevent possible signal interferences.

The main components of the WM-PAS prototype including the QCLs, photoacoustic resonators, electronics, power supply, diaphragm pump and pressure controller were integrated into a box with of size 40×28×14 cm^3 and a weight of 3.2 kg. A photograph of the WM-PAS is shown in Fig. 2.

Each QCL in turn was mounted onto an aluminum alloy shielding and a heat dissipation module which was screwed onto a compact photoacoustic resonator. The electronics integrated the functions of the control of QCLs, system pressure, and lock-in demodulation of the PAS signals were installed right above the resonators. There was a radiation fin designed on the casing of the electronics. The power supply was located next to the electronics to supply power for microphones, electronics, pump and pressure controller. The pump and pressure control were fixed at the bottom of the sensor to control and maintain the designated pressure for gas sample measurement. Also the humidity control including the humidifier and the electronic cold trap were

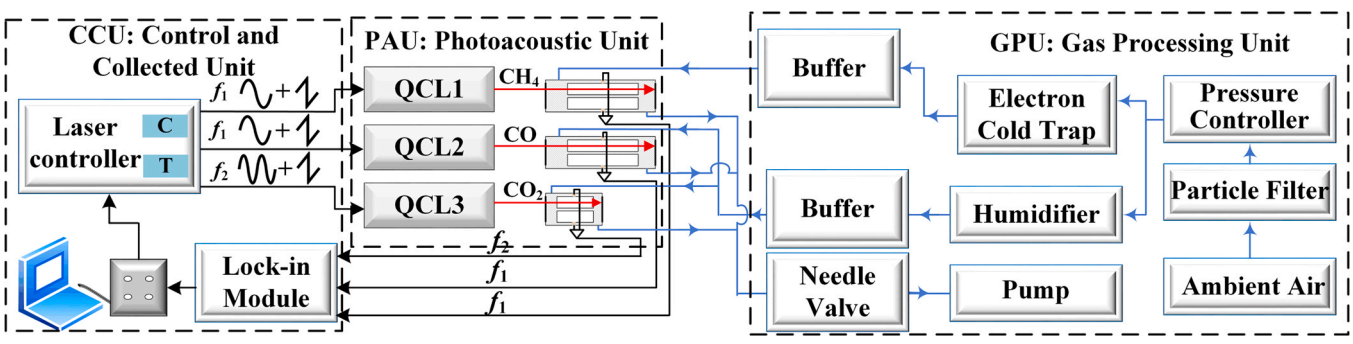

Fig. 1. Structure of the greenhouse gas detection PAS sensor instrumentation.

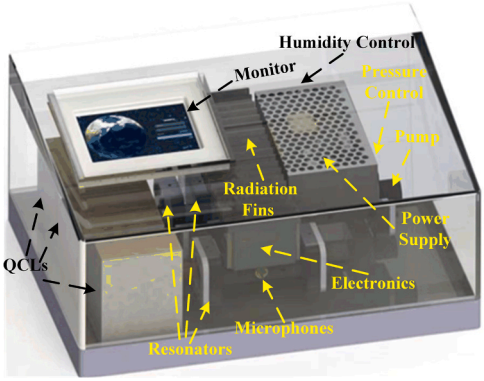

Fig. 2. The integrated WM-PAS prototype.

installed at the back of the sensor, connected to a particle filter as the gas inlet. All the following optimization measurements were completed in the experimental lab with a constant temperature as 25°C.

2.2. Absorption line selection of greenhouse gases

In order to achieve the optimal sensitivities of target gases, the absorption lines considered were optimized within the tunable spectral ranges of the three QCLs. The absorption cross-section simulation results of the three target gases and vapor background given in Hitran2012 [22] at room temperature and atmospheric pressure are presented in Fig. 3. The red lines represent the absorption intensities of the target gases, while the blue lines show the vapor absorption spectra. CH_4 exhibits an uneven absorption spectrum composed of several lines differing both in line-strength and in wavenumber spacing in the 1100 ~ 1500 cm^{-1} region. These absorptions are generated by the energetical dyad ν_b including the ν_2 and ν_4 bending modes. The strongest peak at 1306.12 cm^{-1} (line strength is 6.7×10^{-19} cm/mol) was selected for CH_4 detection. The absorption line located at 2172.76 cm^{-1} corresponding to the R-12 branch of the fundamental ($\Delta\tilde{\nu}=1$) vibrational transition of CO with a line-strength of 2.9×10^{-19} cm/mol was used for CO detection [23]. The characteristic spectral signatures of asymmetric stretching mode (ν_3) of CO_2 [24] generate the absorption around 2347 cm^{-1} shown in Fig. 3(c). For the purpose of balancing sensitivity and saturation concentration, the relatively weak absorption peak at 2345.98 cm^{-1} with a line-strength of 3.8×10^{-18} cm/mol was chosen as the target wavenumber for CO_2 detection. All the designated absorption peaks for the three targets were far away from the strong absorption region of water vapor as depicted in Fig. 3. The other two targets are transparent at the selected absorption line of any detected greenhouse gas. In terms of optical power, we obtained 143 mW at 1306.12 cm^{-1} (CH_4), 175 mW at 2172.76 cm^{-1} (CO) and 56 mW at 2345.98 cm^{-1} (CO_2) for the three QCLs, respectively.

2.3. Photoacoustic resonator design and optimization

Fig. 4 depicts a cross-section of one of the three greenhouse gas detection sensors. Its main components are the QCLs, the resonator and the optical source collection cylinder. The beam outlets of the QCLs are conical, therefore there is a distance (~10 mm) between the beam outlet and the resonator window. In order to avoid the adverse effects of ambient air, especially for CO_2 detection, a N_2 filled tube with the diameter of 3 mm was introduced into that space between the beam outlet and the resonator window for air isolation in the optical path. The differential resonator is made up of two resonance cylinders and buffer volumes located at both ends. Buffer volumes were designed and manufactured with rounded edges and smooth surfaces to avoid dead volumes or local turbulence. The internal face of the resonator was treated by a lapping rod and polishing paste in order to improve its surface quality. The CaF_2 windows (37.8 mm in diameter and 3 mm in depth) were screw fixed between the pressure plates and the buffer volume wall, and sealed by gaskets and O-rings. Two small openings (1.5 mm in diameter) in the middle of the two identical resonator cylinders were drilled for the mounts of the two electret condenser microphones (Type BO6027, Shenzhen Yingge Acoustics Technology®, 115.5 mV/Pa, −19 dB). In order to monitor the humidity and temperature of the resonator, an Omega® (Type HX94) sensor was integrated on the wall of the buffer volume immediately beside the gas outlet. An optical collection cylinder with conical inner shape was located immediately after the resonator for the collection of transmitted optical intensities.

The geometry for the two types differential resonators is shown in Table 1. We use R1 and R2 to represent the two type resonators respectively. The corresponding measured resonant frequencies are 821 Hz (f_1, for CH_4 and CO detection) and 3756 Hz (f_2, for CO_2 detection) respectively, as shown Fig. 5. The details for the geometry optimization design of the resonators are discussed in the Appendix.

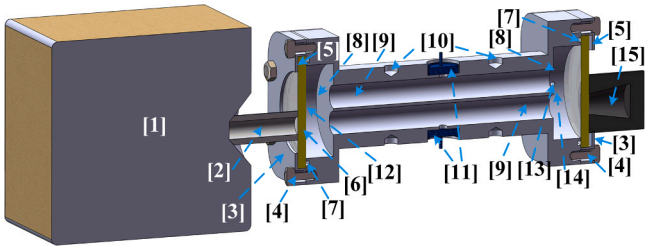

Fig. 4. Cross section of the WM-PAS sensor instrumentation. [1] QCL source, [2] N_2 filled tube, [3] pressure plate, [4] M3 screws, [5] gaskets, [6] CaF_2 windows, [7] O-rings, [8] buffer volume, [9] resonance cylinders, [10] M6 threaded holes, [11] microphones, [12] gas inlet, [13] gas outlet, [14] humidity and temperature sensor, [15] Optical collection cylinder.

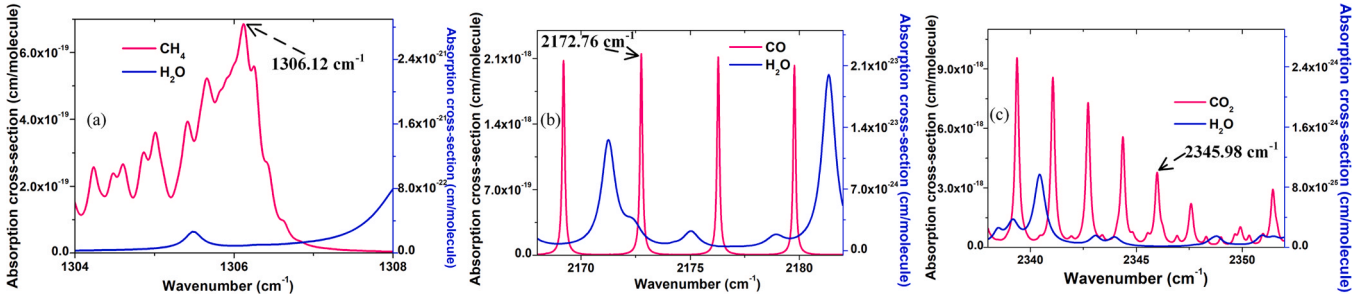

Fig. 3. The absorption characteristics of the three target gases.

Table 1
Parameters of the two differential resonators.

	Type	Resonance cylinder		Buffer volume		Resonance frequency	Target gas
		Length	Diameter	Length	Diameter		
R1	Resonator 1	140 mm	8 mm	30 mm	32 mm	821 Hz (f_1)	CH_4, CO
R2	Resonator 2	40 mm	8 mm	10 mm	20 mm	3756 Hz (f_2)	CO_2

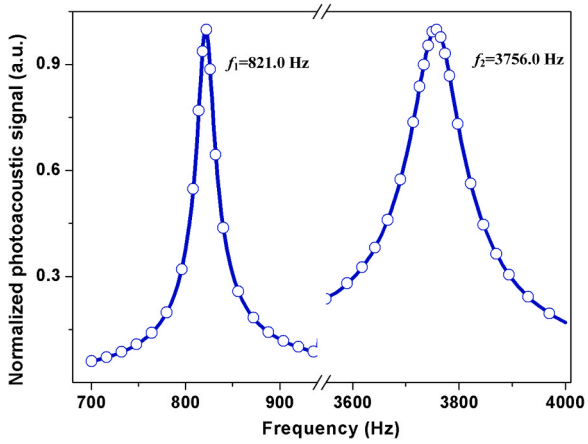

Fig. 5. Resonance frequency responses of the two types of differential resonators.

3. Optimization and evaluation of the photoacoustic sensor

3.1. Optimization of CCU

The selected absorption lines of the three greenhouse gases were targeted by the CCU to operate the QCLs at 28°C (CH_4), 31°C (CO), and 31°C (CO_2), with injection currents 226.0 mA (CH_4), 226.1 mA (CO) and 95.6 mA (CO_2). The modulation depth optimization of the three target gases was implemented by sinusoidal modulation of the three QCL currents at frequencies $f_1/2$ (425.5 Hz) for CH_4 and CO or $f_2/2$ (1878 Hz) for CO_2. The PA amplitude signals could achieve maximum values when the modulation depths of the beams were close to the widths of the absorption lines. The PA amplitude signal responses vs. modulation depths are shown in Fig. 6 which were obtained by measuring the gas samples of 50 ppm CH_4, 15 ppm CO and 200 ppm CO_2 respectively. The optimal modulation depths at the designated wavenumbers were 160 mV (CH_4 at 1306.12 cm^{-1}), 110 mV (CO at 2172.76 cm^{-1}) and 255 mV (CO_2 at 2345.98 cm^{-1}).

3.2. Optimization of the GPU

In this section we aim to discuss the influence of pressure, gas flow rate and humidity on the photoacoustic signal, all of which are controlled by the GPU in Fig. 1. All optimization measurements were acquired with the target gases diluted in N_2.

3.2.1. Pressure effects on signal

The Q-factor of the resonators, the absorption spectrum of the target gases and the V-T relaxation rates vary with pressure, so the pressure optimization in the resonators is a key parameter for PA sensor performance optimization. The two resonator photoacoustic signal dependence on gas pressure were evaluated by measuring the response of R1 to 7 ppm CH_4 and that of R2 to 215 ppm CO_2. The pressure dependence results shown in Fig. 7 were obtained after the modulation depths and modulation frequencies of QCLs were optimized at each designated pressure. The photoacoustic signal of R1 increases nonlinearly with CH_4 pressure as shown in Fig. 7(a). However, as depicted in Fig. 7(b), the photoacoustic signal of R2 rises when the CO_2 pressure is less than 14 PSIG, then the signal reaches a maximum and starts decreasing at higher pressures. Only one pressure controller was used in the WM-PAS sensor, so pressures in *Resonators 1* and *2* were certainly identical. As a result, a gas pressure of 14 PSIG was used as the operating pressure for all three target gas detection measurements.

3.2.2. Gas flow rate effects on signal

The PA signal dependence on gas flow rate was investigated in a range between 0 and 800 sccm, with all other parameters remaining unchanged. The noise levels of the two types of resonators were recorded by measuring signals with N_2 as a reference gas. Fig. 8 shows both PA signals and noise levels. The PA signal response as a function of flow rate was measured using 2 ppm CO, 15 ppm CH_4 and 24 ppm CO_2. It was observed that the PA signal is much less affected by flow rate than by pressure. The CO signal increases with increasing flow rate and reaches a maximum at 600 sccm. A slight monotonic drop occurs with respect to the CH_4 signal with rising flow rate, with total decrease of only 1% signal at 500 sccm compared with that under static conditions. The flow rate has barely any impact on the CO_2 signal with less than 1% deviation between 0 and 800 sccm. The noise level of R1 remained almost unchanged at flow rates smaller than 500 sccm and increased dramatically beyond 600 sccm. R2 shows a similar constant noise level below 700 sccm which increased rapidly to 14 times at 900 sccm. Considering the influence of flow rate on the foregoing PA signals and noise levels of the two resonators, 500 sccm was selected as optimal for the simultaneous measurement of the three greenhouse gases.

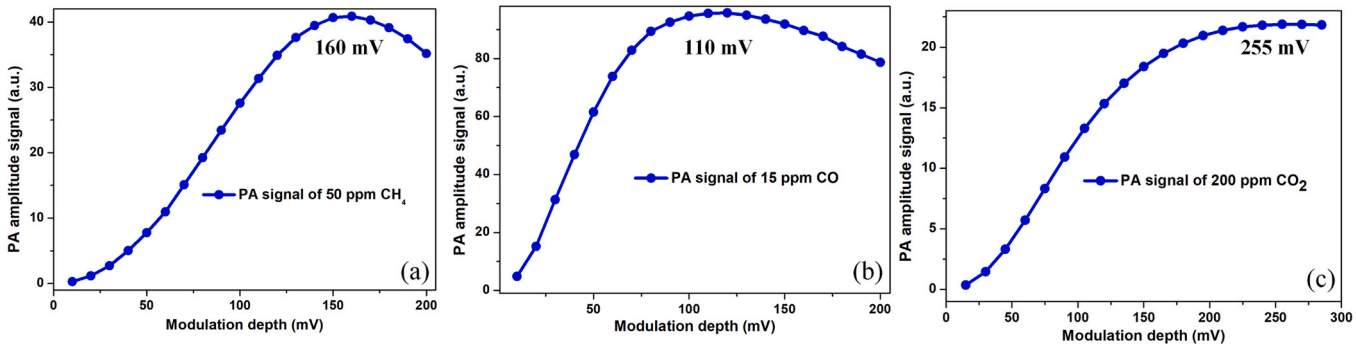

Fig. 6. Modulation depth optimization of the PAS sensor. (a), (b) and (c) PA amplitude signal responses vs. modulation depths for three target gases.

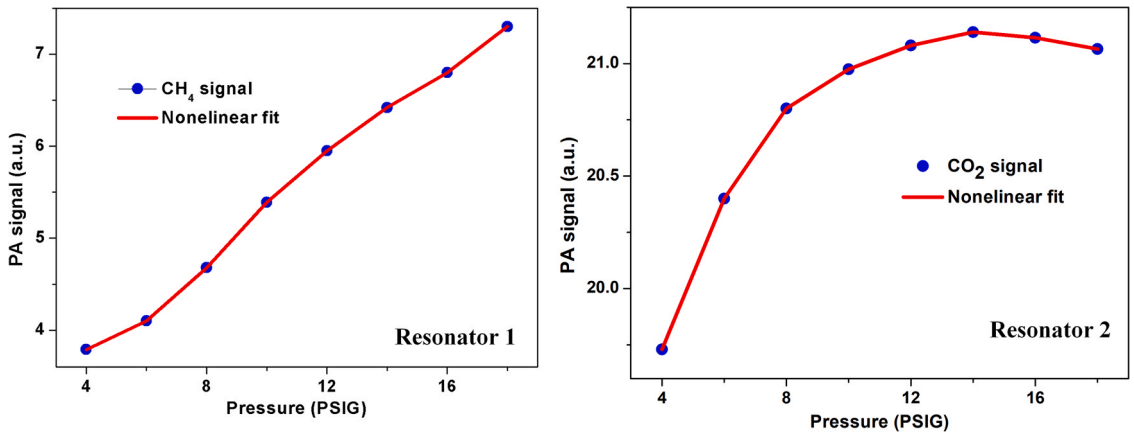

Fig. 7. The relationship between PA signals and gas pressure of the two resonators.

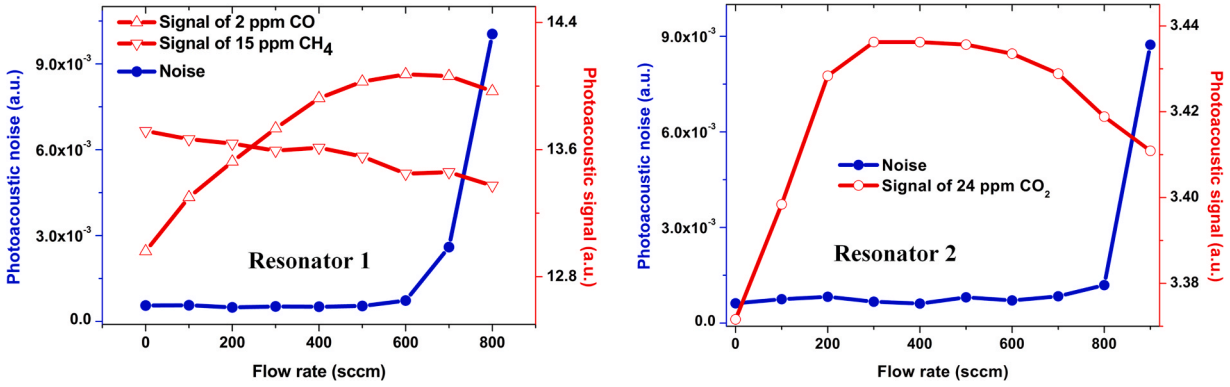

Fig. 8. Influence of flow rate on the PA signals and noise levels for three gases in the two resonators.

3.2.3. Water vapor impact on target gases

Humidity effects on the PA signals of the three greenhouse gases were investigated by measuring the amplitude dependence of 25 ppm CH_4, 10 ppm CO and 432 ppm CO_2 on absolute humidity. Regarding trace concentrations of the three greenhouse gases, their V-T collisions and any vibrational energy back transfer can be neglected.

The results shown in Fig. 9(a) illustrate a signal rise in CH_4 with increased water vapor of 4.2% to reach the maximum at the concentration of 0.36% absolute humidity. This effect was caused by the fact that not all vibrational states excited of CH_4 at the target wavenumber were able to relax completely during one modulation period [9,25,26] without the catalytic effects of water vapor. The collisional relaxation delay is retarded by humidification which partially explains the increase signal in CH_4 at the lower water vapor concentration. The rise in CH_4 signal is also attributed to a fast V-V transition from $CH_4(\nu_b)$ to $H_2O(\nu_2)$ with subsequent V-T-relaxation of water [27]. However, the rising water concentration changes the heat capacity ratio of the gases and deteriorates the Q-factors of the resonators, leading to decreasing signal for CH_4 detection.

CO is a typically slow relaxer and the PA signal is strongly affected by the presence of relaxation promoters in the mixture. Considering CO diluted in N_2 as a first stage, the fastest relaxation process ($\gamma^{VV}_{CO-N_2} \approx 1.4 \times 10^5 s^{-1} atm^{-1}$) is generated by the V-V collision with N_2 since the V-T relaxation of CO into a lower CO energy level is neglected at CO concentrations below 100 ppm [28]. The vibrational energy of CO excited to the ν_1 (around 2172.76 cm^{-1}) state is transferred to N_2 which has a higher resonant ν_1 (2330 cm^{-1}) vibrational level, leading to an endothermic process [23,24]. This relaxation path is promoted by the presence of water vapor. Therefore, a slight decrease for the CO signal occurs first, reaches a minimum at 0.19% humidity, then it increases

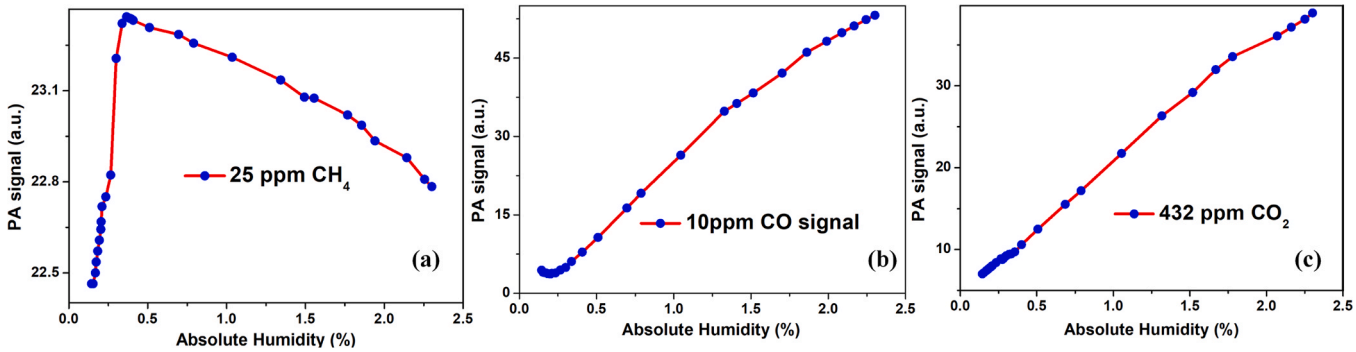

Fig. 9. The influence of humidity on PA signals. (a), (b), (c) represent the PA signal response of CH_4, CO, CO_2 to absolute humidity.

approximately linearly by 14 times up to 2.3% humidity. The reason for the progressive increase is that another new exothermic relaxation process V-V $_{CO\text{-}H2O}$ with a rate of $\gamma^{VV}_{CO-H_2O} \approx 5.5 \times 10^6 s^{-1} atm^{-1}$ [28] dominates as the humidity increases [29].

CO_2 is another typical slow relaxer gas and its signal is also promoted by the efficient catalyst H_2O. The vibrational energy of CO_2 excited to the ν_3 (around 2345.98 cm^{-1}) state respectively is transferred to the ν_1 (2330 cm^{-1}) vibrational level of N_2. The collisional relaxation time of N_2^* level is relatively long, that is to say that a partial energy transfer from the ν_3 state of CO_2 to N_2 is subsequently trapped in a metastable vibrational excited state of N_2 [30]. Therefore, the relaxation process ($\gamma^{VV}_{CO_2-H_2O} \approx 8.5 \times 10^4 s^{-1} atm^{-1}$) in a dry CO_2 mixture is relatively slow, resulting in a weak PA signal [31]. The presence of water vapor adds an additional relaxation path [32] which is generated by the V-V collisional energy exchange between CO_2 and H_2O molecules ($\gamma^{VV}_{CO_2-H_2O} \approx 2.3 \times 10^7 s^{-1} atm^{-1}$) and is proportional to the humidity level [33]. This mechanism can explain the fact that the CO_2 PA signal in Fig. 9(c) shows a linear response to the absolute humidity and becomes enhanced by 4.4 times under 2.3% humidity.

3.3. Performance evaluation of photoacoustic sensor

3.3.1. PA setup simplification and sensitivity evaluation

For the purpose of PA noise level evaluation, the two types of resonators were filled up with N_2 and the PA responses were measured under incident radiation as shown in Fig. 1. The noise levels at the resonators shown in Fig. 10 were calculated as the standard deviation (σ) of collected PA data over 150 s. The first and second numbers shown in the insets of Fig. 10 represent the accumulation number and averaging time, respectively. The noise level magnitudes of both resonators were on the order of 10^{-3} (a.u.).

As compactness and less complexity is an essential step toward greenhouse gas detection in ambient air for real world PA applications, it was inconvenient to install humidity control equipment in the gas monitoring sensor compartment. So, we simplified the experimental apparatus, and only used an electronic cold trap and washing bottle to achieve gas drying and humidification as shown in Fig. 1. The washing bottle was in a temperature-controlled water bath (25°C). Such design contributes a constant humidity in the resonators, resulting in the enhancement of PA signals and instability suppression due to the achieved absence of humidity variations: It was found that the water concentration of the sample filtered by the electronic cold trap was maintained unchanged at 0.29%. After the gas sample was passed through distilled water in the washing bottle, the humidity was 2.3% and the water vapor concentration generated by such humidification method was dependent on the ambient dew point and saturation vapor pressure.

Fig. 9 shows that the CH_4 PA signal value with 0.29% humidity is somewhat greater than that with the absolute humidity at 2.3%. And obviously, the photoacoustic signals of CO and CO_2 are enhanced by introducing humidification as shown in Fig. 9(b) and (c). Therefore, for practical field use, the CH_4 gas sample was dried by the electronic cold trap, while CO and CO_2 gases were passed through a gas washing bottle filled with distilled water before letting into the resonators.

To evaluate the performance of the WM-PAS sensor, the system was operated with the foregoing optimized parameters. Samples of 25 ppm CH_4, 15 ppm CO and 100 ppm diluted in N_2 were measured after introducing humidification by passage (bubbling) through distilled water. Then the humidified samples were dried by the electronic cold trap and the photoacoustic signals of the humidified and dried samples were detected. As shown in Fig. 11(a), the signal from 25 ppm CH_4 dried in the electronic cold trap is 10% greater than the humidified value as marked by the dashed ellipse. The signals from 15 ppm CO and 100 ppm CO_2 are improved by 11.2 and 6.7 times, respectively, under humidity conditions, Fig. 11(b) and (c).

The results shown in Fig. 11 were observed with an averaging time of 1 s after removing the constant background signal with N_2. The PA amplitude values from 25 ppm CH_4, 15 ppm CO and 100 ppm CO_2 at the target wavenumbers were 23.156 (a.u.), 94.921 (a.u.) and 11.421 (a.u.), respectively. With an averaging time as 1 s, the noise floors of the two resonators were found to be 5.517×10^{-3} (R1) and 1.914×10^{-3} (R2) as shown in Fig. 10. Therefore, the limits of detection (LoD) of the WM-PAS sensor were 5.6 ppb for CH_4, 0.8 ppb for CO and 17.2 ppb for CO_2 with 1-

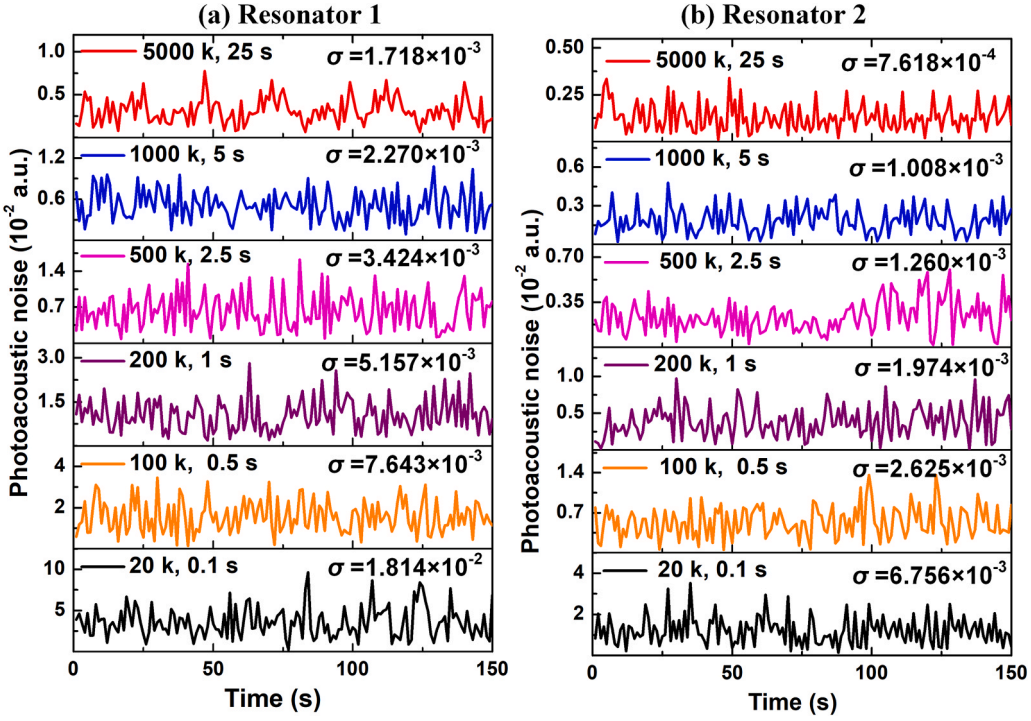

Fig. 10. Photoacoustic noise level analysis of the two resonators.

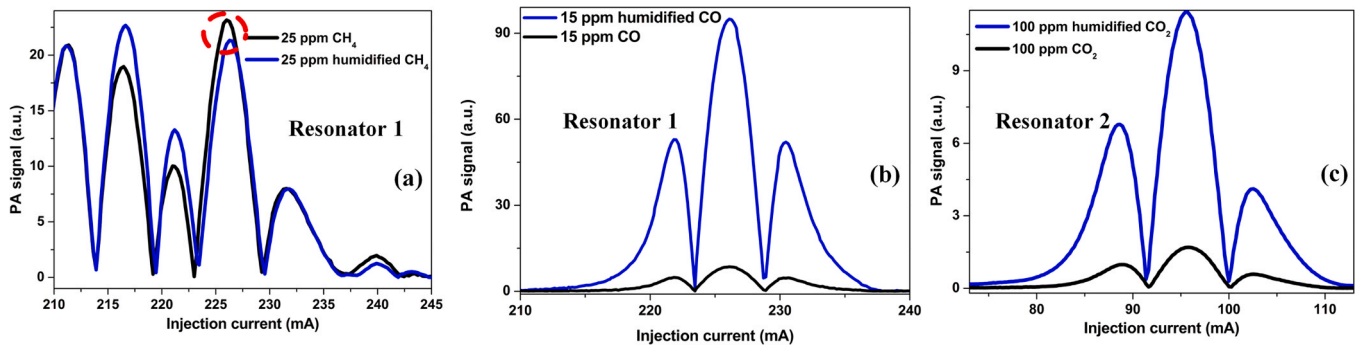

Fig. 11. The 2 f spectra of the three target gases. (a), (b), (c) are the PA signals of the three target gases filtered with electron cold trap and humified with washing bottle, respectively.

s averaging time.

With the longer averaging time, the noise level of the two types of resonators dramatically decreased as expected. Longer averaging times can be set by the CCU integrated in this sensor, if sensitive LoDs are required in specific cases. For example, with an averaging time of 5 s, the LoDs will be 2.3 ppb (CH_4), 0.4 ppb (CO) and 7.1 ppb (CO_2), respectively.

3.3.2. *Dynamic performance evaluation of the PA sensor*

The dynamic range for greenhouse gas monitoring of the WM-PAS sensor was identified by testing the PA response of the target gases with different concentrations in the range of several ppb to a few hundred ppm. The results are presented in Fig. 12. The signals from both CH_4 and CO gases exhibit a linear response in the concentration range from ppb to tens of ppm. The signal from CO_2 increases linearly with concentration in the range $\leq$350 ppm, but then it becomes nonlinear with concentration increase without saturation. The saturation concentration occurred at the CO_2 concentration of 1000 ppm. A decreasing signal appeared after the saturation effect and the detailed reason for this phenomenon was given in Appendix. This sensor is suitable for the CO_2 detection in the range of 0–1000 ppm due to a non-monotonic response throughout the entire range. The dynamic range of the WM-PAS sensor for the detection of the three greenhouse gases was found to be more than 6 orders of magnitude.

We also tested the PA signal responses with the target gas concentrations diluted in air with the designated humidity (0.29% for CH_4 and 2.3% for CO and CO_2) for the purpose of atmospheric monitoring calibration. With the ambient air as background gas, the resonance frequencies of the R1 and R2 resonators moved lower to 805 Hz and 3686 Hz respectively. The detection results are shown in Fig. 13. The CH_4 PA signals with the air with 0.29% humidity were almost identical with the CH_4 data diluted in 0.29% humidity N_2 which were depicted in Fig. 12(a). The CO PA signal diluted in air with the humidity of 2.3% is about 12% lower than those values diluted by N_2 with the same humidity. The CO_2 PA signals were enhanced approximately 26.3% by the presence of 2.3% humidity air.

4. *In situ* monitoring of atmospheric greenhouse gases

The results of greenhouse gas monitoring in the field are presented in Fig. 13 with the WM-PAS sensor located in an observation station in the Qinling National Botanical Garden, which is the world's largest with an area of 639 square kilometers. Qinling National Botanical Garden is located in the northern slope of Qinling Mountains, about 70 kilometers south of downtown Xi'an and it is between 108° 13'~108° 29' E longitude and 33° 43'~34° 04' N latitude. With an altitude variation of over 2500 m, Qinling National Botanical Garden is known as the "biological gene bank" of China, and has one of the most diversified plants and clearest vegetation zones all over the world.

The observation station was located in a forested site in central China. In order to quantify and address the adverse effects of local human transportation activities and vehicles, gas samples were extracted in ambient air at an elevation of 15 m above ground by the tube connection from a 30 m high tower. The designed WM-PAS sensor and a commercial instrument (Model G2401, Picarro®, USA) which is based on the Cavity Ring-Down Spectroscopy (CRDS) technology principle [34] were placed together in an air-conditioned room maintained at the constant temperature of 25°C. The atmospheric relative humidity was about 71%. The extracted gas sample An electronic cold trap was also placed upstream to the Picarro instrument for the purpose of dehumidification. CRDS provides a basic way to enhance the light-gas molecular interaction by at least thousand fold with a small sample length, and it employs time-domain signals. Therefore, the CRDS signal is insensitive to the laser intensity fluctuation [35]. Nevertheless, the limitation of CRDS technique is the requirement of high-reflectivity mirrors to form an optical cavity, but the reflectivity coatings are usually available in a short wave length range, which limits the working spectral range for a particular configuration of mirror cavity [34].

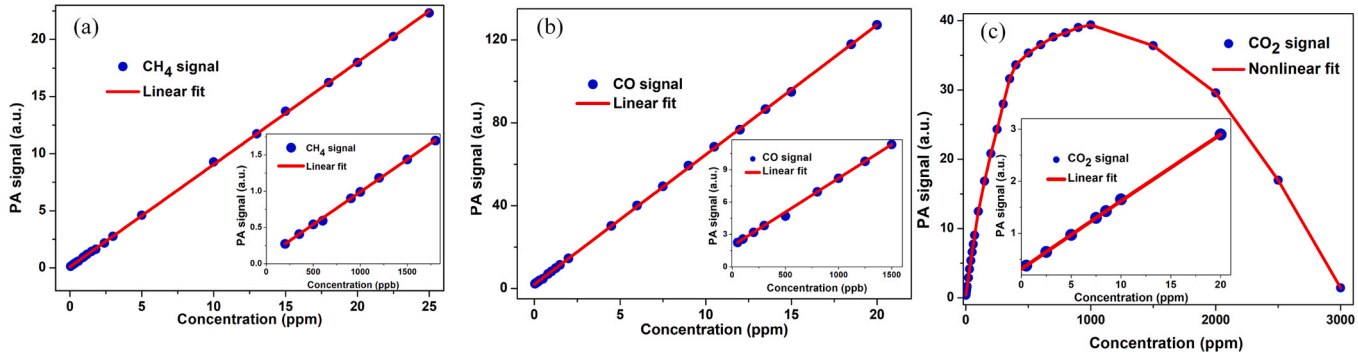

Fig. 12. The photoacoustic responses of the three target gases v.s. concentration diluted in N_2.

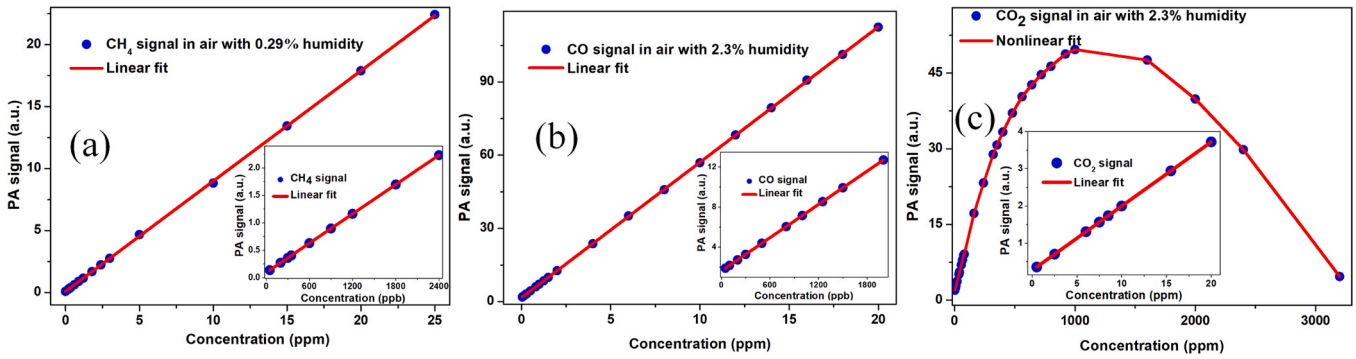

Fig. 13. The photoacoustic responses of the three target gases v.s. concentration diluted in air.

Moreover, precise alignment of the mirror cavity is required to achieve the mode-matching condition. So the instability of the mode-matching optics and electrical components may degrade CRDS signals [35]. Such high-quality demand of reflectivity coating indeed greatly increases the difficulty and cost of CDRS based instrument. The minimal averaging time available for G2401 used in our measurements was 1 s, and the corresponding LODs (1σ) were 0.1 ppb (CH_4), 3.5 ppb (CO) and 17 ppb (CO_2), respectively. With an averaging time of 5 s, the LoDs of our PA sensor are 2.3 ppb (CH_4), 0.4 ppb (CO) and 7.1 ppb (CO_2), respectively, with comparable detection sensitivities, the PA sensor has demonstrated efficient multiple greenhouse gas monitoring capabilities.

With 1-s averaging time, the WM-PAS sensor performed in excellent agreement with the results obtained from the CRDS based G2401 instrument as shown in Fig. 14. The concentration calibrations were calculated with the concentration dependent PA signals of three target greenhouse gases diluted in air with the optimized humidity. The average ambient concentration of CH_4, the gas with the minimal fluctuation among the three greenhouse gases during the five days of trials, was 2.1 ppm. Diurnal variations in CH_4 emissions have been reported to fluctuate significantly, depending on the mountain ecosystem [36]. The maximum concentration of CH_4 was registered at midnight while the minimum was observed in the daytime. The mean CO observed during the five days ranged between 302 ppb and 375 ppb. From midnight to early morning, a sharp increase in CO was observed as the consequence of CO emitting sources, like local traffic, as suggested by the concomitant enhancements of black carbon and other combustion products [37]. Mud carrying trailers are responsible for this phenomenon because they are only allowed to drive on Chinese roads between 0:00–8:30 (local time) daily. The average concentration of CO_2 in the five measurement days was 432 ppm. The daily cycle of CO_2 was mostly dominated by vegetation gas exchange activities [38].

5. Conclusions

A robust and compact WM-PAS sensor for greenhouse gas monitoring was established and tested in this work. Three QCLs designated for CH_4, CO and CO_2 detection, respectively, were used as the excitation sources and three differential resonators with two dimensions were optimally designed in terms of gas detection sensitivity and saturation concentration measurements. FPGA designed circuits integrated in this sensor resulted in good performance with laser modulation and digital orthogonal vector type lock-in demodulation. The integrated WM-PAS sensor was demonstrated to be capable of high sensitivity and wide dynamic range detection combined with QCLs and differential resonators. Ambient parameters with the potential to cause cross-interference (gas flow rate and pressure as well as humidity) were investigated and optimized. With the optimal parameters, the integrated WM-PAS sensor exhibited minimum LoDs: 5.6ppb for CH_4, 0.8 ppb for CO and 17.2 ppb for CO_2 with the averaging time as 1 s. The dynamic range of this portable greenhouse detection sensor was found to be greater than 6

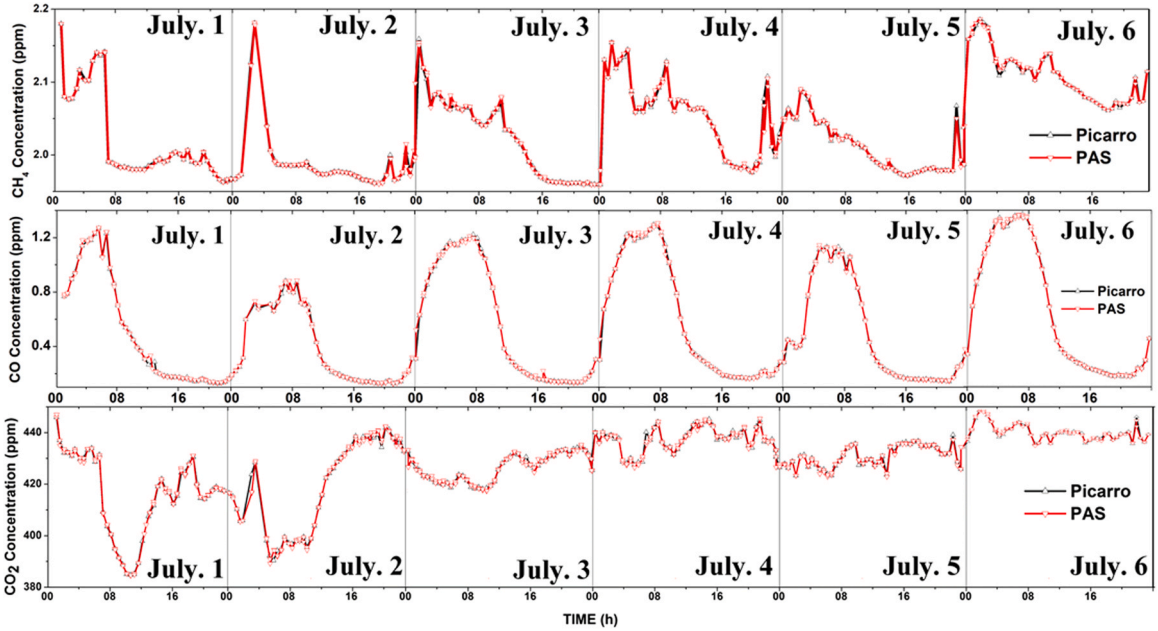

Fig. 14. Continuous monitoring of greenhouse gases in Qinling National Botanical Garden, China.

orders of magnitude. The continuous monitoring capability of the sensor was demonstrated by continuously measuring the ambient air over one week in an outdoors observation station. The results were validated and showed excellent agreement with simultaneous data obtained using a commercial CRDS based instrument (G2401, Picarro®), located at the same site. Thanks to the advantages of high sensitivity, large dynamic range and stable monitoring, the WM-PAS sensor with the three integrated QCLs, three differential resonators, and FPGA based circuits, can be employed in the field of greenhouse gas detection for real-time monitoring of chemical reactions and gas pollutants in the atmosphere.

CRediT authorship contribution statement

Xukun Yin: Validation. **Baisong Chen:** Validation. **Xiaopeng Shao:** Supervision. **Lixian Liu:** Writing – review & editing, Writing – original draft, Methodology. **Huiting Huan:** Methodology. **Andreas Mandelis:** Writing – review & editing, Supervision. **Jinsong Zhan:** Software. **Shaowei Jiang:** Software, Resources. **Xueshi Zhang:** Data curation. **Le Zhang:** Formal analysis.

Declaration of Competing Interest

The authors declare that they have no known competing financial interests or personal relationships that could have appeared to influence the work reported in this paper.

Data availability

Data will be made available on request.

Acknowledgments

The authors are grateful to the National Natural Science Foundation of China (Grant Nos. 62350710213, 62175194 and 62271370). AM also gratefully acknowledges a Discovery fund from the Natural Sciences and Engineering Research Council of Canada and to Canada Foundation for Innovation (CFI) JELF program. This work was also supported by the Fundamental Research Funds for the Central Universities (Grant Nos. QTZX23081 and QTZX23069). We also acknowledge the Concept Grant of Hangzhou Institute of Technology of Xidian University (No. GNYZ2023XJ0203). L. Liu acknowledges the Natural Science Foundation of Shaanxi Province (Grant No. 2023-YBSF188). This research was also supported by the Baima Lake Laboratory Joint Funds of the Zhejiang Provincial Natural Science Foundation of China under Grant No. LBMHZ24F050003.

Appendix

The differential resonators fabricated in the WM-PAS sensor were used for greenhouse gas monitoring. Therefore, the gas detection range was determined by the concentrations of three target gases (CH_4, CO and CO_2) in the ambient air. The concentration of CH_4 and CO is usually at ppm levels in ambient air, therefore the optical absorption length of the incident beam had to be extended to achieve acceptable gas sensitivity. In terms of these two-gas detection operations, the length and diameter of the resonant cylinders was 140 mm and 8 mm, respectively, while the length and diameter of the buffer volumes at the two ends of the resonant cylinder was set at 30 mm and 32 mm, respectively. Figs. A1 and A2 show the PA responses vs. three target gases by concentrations using Finite Element Method (FEM) software COMSOL Multiphysics ® v6.0. Fig. A1(a) and (b) show the simulated PA signal results from CH_4 and CO at the designated wavenumbers of 1306.12 cm^{-1} (CH_4) and 2172.76 cm^{-1} (CO), respectively. The PA signals from both gases increase linearly with concentration without saturation appearance, so the simulated results show that such a dimensional differential resonator is adequate for CH_4 and CO detection in the atmosphere.

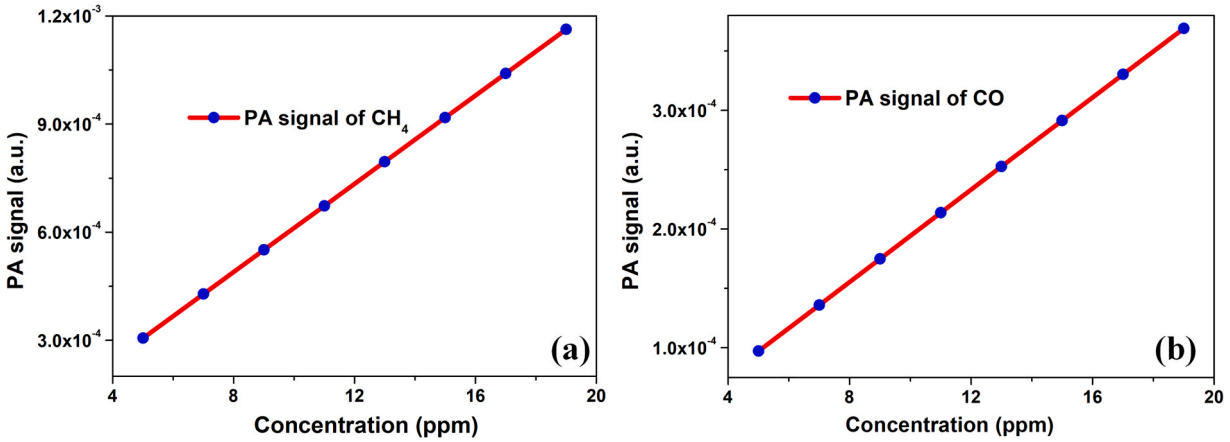

Fig. A1. Simulated PA signal v.s. target gas concentration. (a): CH_4 (b): CO.

The CO_2 concentration in the ambient air is usually between 300 ppm ~ 1000 ppm (forest region: 300–450 ppm; city region: ~500 ppm; empty room: 500–700 ppm; stuffy bedroom: 700–1000 ppm). Moreover, the infrared absorption line (the line-strength of 3.8×10^{-18} cm/mol at 2345.98 cm^{-1}) is about 5 times stronger than that of the other two target gases. Therefore, the shorter differential resonator is necessary in order to avoid the absorption saturation occurrence. In the CO_2 PA response simulation, the length and diameter of the buffer volume and the diameter of the resonant cylinder were set as constants at 10 mm, 20 mm and 8 mm, respectively. The length of the resonant cylinder was varied from 30 mm to 70 mm. The various color curves in Fig. A2 represent the simulated PA response with different optical absorption lengths (the total length of the resonant cylinder and buffer volume). The saturation concentrations for the optical absorption lengths of 90 mm, 80 mm and 70 mm are 750 ppm, 800 ppm and 930 ppm respectively, which are lower than or close to the upper concentration limit of CO_2 in the ambient environment to be tested. The signal with 60 mm optical absorption length shows the maximal PA response and its saturation concentration is greater than 1000 ppm which can be adequate for atmospheric CO_2 detection. The saturation concentration with 50 mm optical absorption length is 1400 ppm, which is lower than the PA value with 60 mm optical absorption length at the CO_2 range of ambient air. Therefore, the dimensions of the resonator (R2 for CO_2 detection in

terms of length and diameter of buffer volume were set at 10 mm and 20 mm, and the length and diameter of the resonant cylinder at 40 mm and 8 mm, respectively. The simulated results showed a good agreement with the experimental dynamic range for CO_2 detection which was presented in Fig. 12(c). Therefore, the simulated results regarding to the saturation concentration and resonance frequency exhibited a valuable evidence for the optimization design of the resonators.

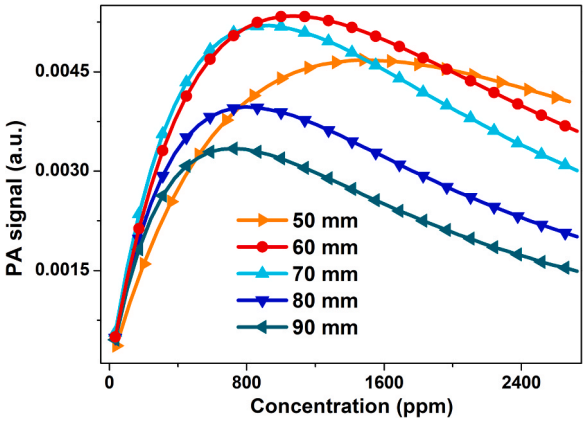

Fig. A2. Determination of optimal resonator length for CO_2 detection.

Fig. A2 describes an interesting phenomenon for the decreasing PA signal with higher CO_2 concentration beyond the saturation concentration. The effect can be explained by the effective coupling efficiency between the incident beam and normal node pressure [39]. The PA amplitude signal $A(\omega)$ can be represented as [39]

$$A(\omega) = -\frac{\alpha Q(\gamma-1)}{\omega V_c} P_I, P_I = \int p(\vec{r}) I\left(\vec{r}, \omega\right) dV \tag{A1}$$

where $\omega=2\pi f$ is the resonance angular frequency, α is the beam absorption coefficient (cm^{-1}), Q is the quality factor of the resonator, γ is the ratio of specific heats of the target gas ($\gamma=C_p/C_v$, C_p and C_v is the specific heat of the gas at constant pressure and volume, respectively), and V_c is the resonator volume. $_{PI}$ represents the effective coupling efficient, which is the integration of normal node pressure $p(\vec{r})$ and beam distribution $I(\vec{r}, \omega)$ generated by the target gas absorption. $\vec{r}$ represents coordinate location in the differential resonator.

Based on the full linearized Navier-Stokes (FLNS) formulation [40], the thermal-acoustic model of the differential resonators was solved using the software COMSOL, which rigorously takes into account surfaces and volume losses, at the price of higher calculation cost. The geometrical parameters were selected as the dimensions of the shortest absorption length shown in Fig. A2. The normal node pressure distribution of the differential resonator could be calculated through the eigenfrequency choice in the COMSOL software and the results are shown in Fig. A3(a) with the simulated resonant frequency. The left and right column illustrations of Fig. A3 show the 2-D and x-axis distributions of the normal node pressure, respectively.

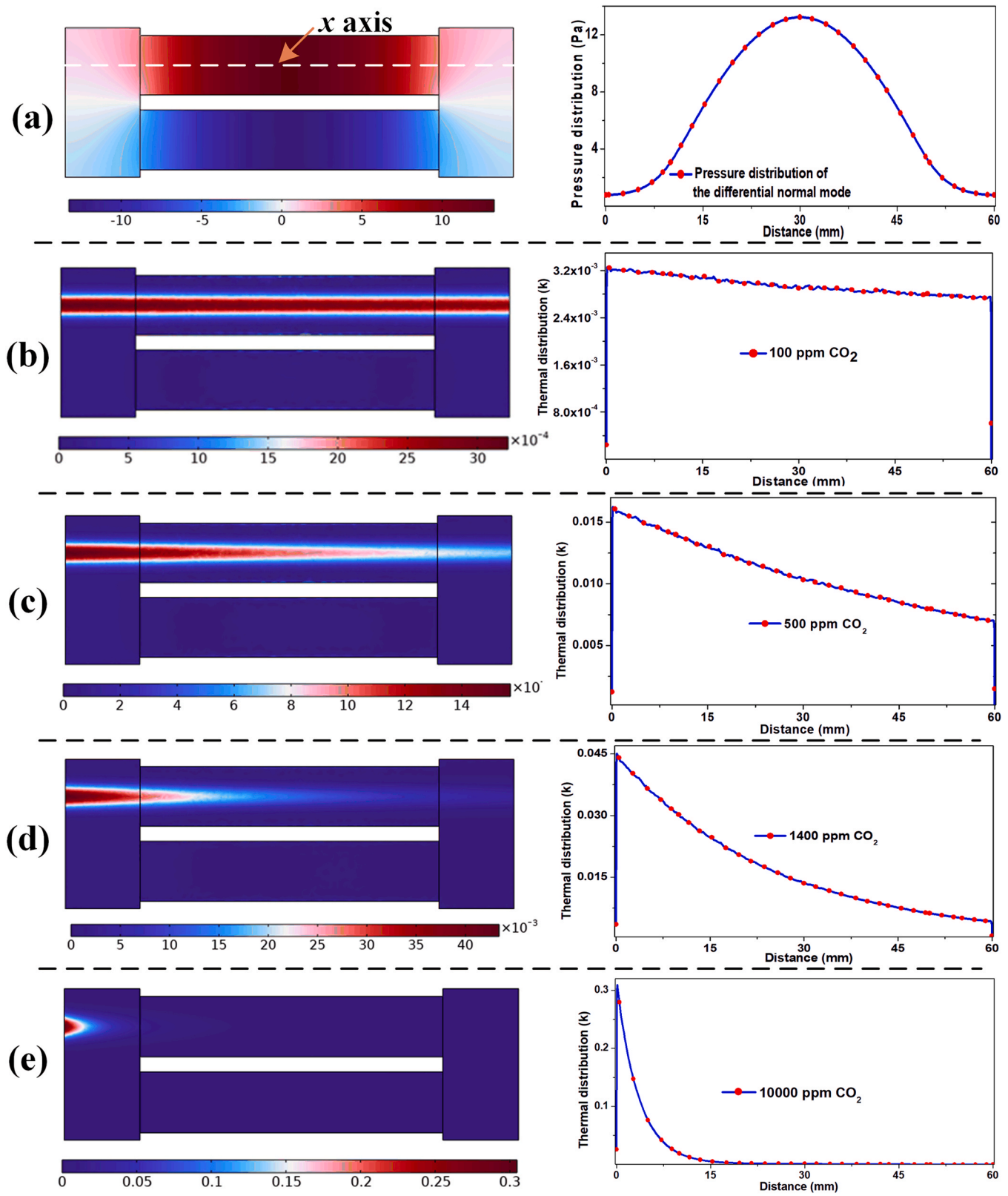

Fig. A3. Simulated results for the differential resonator. (a): the distribution of normal node pressure; (b)~(e) the optical distributions with different CO_2 concentration.

Within this framework, based on the Lambert-Beer law, a Gaussian thermal source I_T (shown in Eq. (A2)) was used to imitate the incident beam through the differential resonator.

$$I_T = I_0 e^{-\alpha_{co_2} cx} e^{-r^2/a^2} \alpha_{co_2} c \tag{A2}$$

where α_{CO2} is the absorption coefficient (94.2 cm^{-1}) at the target wavenumber 2345.98 cm^{-1} of pure CO_2 and c is CO_2 concentration. The beam propagates along the x-axis. a is the waist radius of the Gaussian beam, r represents the distance from the center axis along the beam cross-section. The simulated results of the thermal source are depicted in Fig. A3(b) ~ (e) in with 100 ppm, 500 ppm, 1400 ppm and 10,000 ppm CO_2, respectively. The left and right column illustrations show the 2-D and x-axis distributions of the thermal source respectively. The beam distribution within the differential resonator is seen to be significantly affected by the CO_2 concentration. With 100 ppm CO_2, the beam propagates across the entire resonator. When the concentration increases to 500 ppm, the beam mainly focuses on the first buffer cylinder and resonance cylinder. It reaches 1400 ppm, with almost only the first buffer cylinder excited. When the concentration reaches 10,000 ppm, only the target gas around the window is responsible for light absorption.

The PA signal $|A_d(\omega)|$ (shown in Eq. (A3)) is proportional to the sum of the discrete values of normal node pressure $p_i(\vec{r}_i)$and thermal beam $I_i(\vec{r}_i, \omega)$shown in Fig. A3.

$$|A_d(\omega)| = \frac{\alpha Q(\gamma - 1)}{\omega V_c} \sum_{i=1}^{M} p_i(\vec{r}_i) I_i(\vec{r}_i, \omega) \tag{A3}$$

The calculated PA signal response to CO_2 concentration is shown in Fig. A4, which is consistent with Fig. A2. The effective coupling efficient between the normal node pressure of the resonator and incident beam distribution as well as the dynamic ranges of the target gases are of great importance to the measurements and need to be further considered in the resonator design.

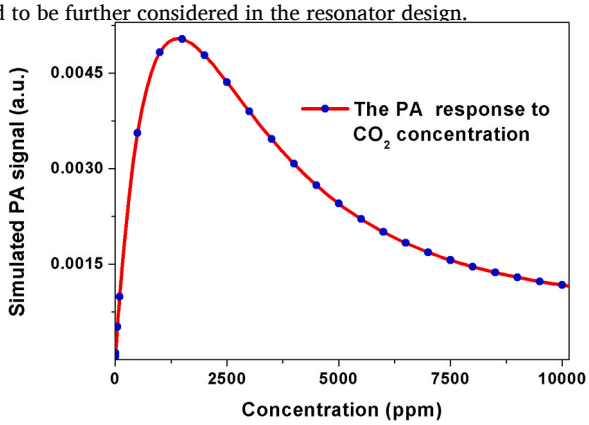

Fig. A4. The simulated PA response to CO_2 concentration.

References

[1] United Nations Framework Convention on Climate Change, INDCs as Communicated by Parties, 2015. http://www4.unfccc.int/submissions/indc/Submission%20Pages/submissions.aspx.

[2] M. Omara, M.R. Sullivan, L. Xiang, R. Subramanian, A.L. Robinson, A.A. Presto, Methane emissions from conventional and unconventional natural gas production sites in the Marcellus shale basin, Environ. Sci. Technol. 50 (2016) 2099–2107.

[3] T. Dixon, K.D. Romanak, Improving monitoring protocols for CO_2 geological storage with technical advances in CO_2 attribution monitoring, Int. J. Greenh. Gas Control 41 (2015) 29–40.

[4] D. Ehhalt, M. Prather, F. Dentener, R. Derwent, E. Dlugokencky, Atmospheric Chemistry and Greenhouse Gases. Climate change 2001: The Scientific Basis, Intergovernmental Panel on Climate Change, 2001.

[5] A. Feitz, I. Schroder, F. Phillips, T. Coates, K. Negandhi, S. Day, A. Luhar, S. Bhatia, G. Edwards, S. Hrabar, E. Hernandez, B. Wood, T. Nylor, M. Kennedy, M. Hamilton, M. Hatch, J. Malos, M. Kochanek, P. Reid, J. Wilson, N. Deuscher, S. Zegelin, R. Vincent, S. White, C. Ong, S. George, P. Maas, S. Towner, N. Wokker, D. Griffith, The Ginninderra CH_4 and CO_2 release experiment: an evaluation of gas detection and quantification techniques, Int. J. Greenh. Gas Control 70 (2018) 202–224.

[6] L. Dong, F.K. Tittel, C. Li, N.P. Sanchez, H. Wu, C. Zheng, Y. Yu, A. Sampaolo, R. J. Griffin, Compact TDLAS based sensor design using interband cascade lasers for mid-IR trace gas sensing, Opt. Express 24 (2016) A52.

[7] N. Lang, U. Macherius, M. Wiese, H. Zimmermann, J. Ropcke, J.H. van Helden, Sensitive CH_4 detection applying quantum cascade laser based optical feedback cavity-enhanced absorption spectroscopy, Opt. Express 24 (2016) 536–543.

[8] S. Kassi, M. Chenevier, L. Gianfrani, A. Salhi, Y. Rouillard, A. Ouvrard, D. Romanini, Looking into the volcano with a mid-IR DFB diode laser and cavity enhanced absorption spectroscopy, Opt. Express 14 (2006) 11442–11452.

[9] J. Peltola, M. Vainio, T. Hieta, J. Uotila, S. Sinisalo, M. Metsälä, M. Siltanen, L. Halonen, High sensitivity trace gas detection by cantilever-enhanced photoacoustic spectroscopy using a mid-infrared continuous-wave optical parametric oscillator, Opt. Express 21 (8) (2013) 10240–10250.

[10] S.D. Qiao, Y. He, H.Y. Sun, P. Patimisco, A. Sampaolo, V. Spagnolo, Y.F. Ma, Ultra-highly sensitive dual gases detection based on photoacoustic spectroscopy by exploiting a long-wave, high-power, wide-tunable, single-longitudinal-mode solid-state laser, Light Sci. Appl. (2024), https://doi.org/10.1038/s41377-024-01459-5.

[11] K. Chen, S. Liu, B. Zhang, Z. Gong, Y. Chen, M. Zhang, H. Deng, M. Guo, F. Ma, F. Zhu, Q. Yu, Highly sensitive photoacoustic multi-gas analyzer combined with mid-infrared broadband source and near-infrared laser, Opt. Laser Eng. 124 (2020) 105844.

[12] K. Liu, J. Mei, W. Zhang, W. Chen, X. Gao, Multi-resonator photoacoustic spectroscopy, Sens. Actuators B Chem. 251 (2017) 632–636.

[13] Y. Liu, S. Qiao, C. Fang, Y. He, H. Sun, J. Liu, Y. Ma, A highly sensitive LITES sensor based on a multi-pass cell with dense spot pattern and a novel quartz tuning fork with low frequency, Opto-Electron. Adv. 7 (3) (2024) 230230.

[14] Y. Cao, R. Wang, J. Peng, K. Liu, W. Chen, G. Wang, X. Gao, Humidity enhanced N2O photoacoustic sensor with a 4.53 μm quantum cascade laser and Kalman filter, Photoacoustics 24 (2021) 100303.

[15] Y. Cao, Q. Liu, R. Wang, K. Liu, W. Chen, G. Wang, X. Gao, Development of a 443 nm diode laser-based differential photoacoustic spectrometer for simultaneous measurements of aerosol absorption and NO_2, Photoacoutics 21 (2021) 100229.

[16] Y. Ma, R. Lewicki, M. Razeghi, F.K. Tittel, QEPAS based ppb-level detection of CO and N_2O using a high power CW DFB-QCL, Opt. Express 21 (1) (2013) 1008–1019.

[17] L. Liu, H. Huan, A. Mandelis, L. Zhang, C. Guo, W. Li, X. Zhang, X. Yin, X. Shao, D. Wang, Design and structural optimization of T-resonators for highly sensitive photoacoustic trace gas detection, Opt. Laser Technol. 148 (2022) 107695.

[18] C. Fang, T. Liang, S. Qiao, Y. He, Z. Shen, Y. Ma, Quartz-enhanced photoacoustic spectroscopy sensing using trapezoidal- and round-head quartz tuning forks, Opt. Lett. 49 (3) (2024) 770–773.

[19] L. Liu, A. Mandelis, H. Huan, K.H. Michaelian, step-scan differential Fourier transform infrared photoacoustic spectroscopy (DFTIR-PAS): a spectral deconvolution method for weak absorber detection in the presence of strongly overlapping background absorptions, Opt. Lett. 42 (7) (2017) 1424–1427.

[20] Z. Lang, S. Qiao, Y. Ma, Fabry–Perot-based phase demodulation of heterodyne light-induced thermoelastic spectroscopy, Light Adv. Manuf. 4 (2023) 23.

[21] L. Liu, H. Huan, X. Zhang, L. Zhang, X. Shao, A. Mandelis, L. Dong, Laser induced thermoelastic contributions from windows to signal background in a photoacoustic cell, Photoacoustics 22 (2021) 100257.

[22] L.S. Rothman, D. Jacquemart, A. Barbe, D. Chris Benner, M. Birk, L.R. Brown, M. R. Carleer, C. Chackerian, K. Chance, L.H. Coudert, V. Dana, V.M. Devi, J.-M. Flaud, R.R. Gamache, A. Goldman, J.-M. Hartmann, K.W. Jucks, A.G. Maki, J.-Y. Mandin, S.T. Massie, J. Orphal, A. Perrin, C.P. Rinsland, M.A.H. Smith, J. Tennyson, R.N. Tolchenov, R.A. Toth, J. Vander Auwera, P. Varanasi, G. Wagner, The Hitran 2004 molecular spectroscopic database, J. Quant. Spectrosc. Radiat. Transf. 96 (2) (2005) 139–204.

[23] F. Sgobba, A. Sampaolo, P. Patimisco, M. Giglio, G. Menduni, A.C. Ranieri, C. Hoelzl, H. Rossmadl, C. Brehm, V. Mackowiak, D. Assante, E. Ranieri, V. Spagnolo, Compact and portable quartz-enhanced photoacoustic spectroscopy

sensor for carbon monoxide environmental monitoring in urban areas, Photoacoustics 25 (2022) 100318.
[24] P.S.R. Prasad, K.S. Prasad, N.K. Thakur, FTIR signatures of type-II clathrates of carbon dioxide in natural quartz veins, Curr. Sci. (2006) 1544–1547.
[25] L. Zhang, L. Liu, X. Zhang, X. Yin, H. Huan, H. Liu, X. Zhao, Y. Ma, X. Shao, T-type cell mediated photoacoustic spectroscopy for simultaneous detection of multi-component gases based on triple resonance modality, Photoacostics 31 (2022) 100492.
[26] T. Liang, S. Qiao, Y. Chen, Y. He, Y. Ma, High-sensitivity methane detection based on QEPAS and H-QEPAS technologies combined with a self-designed 8.7 kHz quartz tuning fork, Photoacoustics 36 (2024) 100592.
[27] N. Barreiro, A. Peuriot, G. Santiago, V. Slezak, G. Santiago, Glomae, Water-based enhancement of the resonant photoacoustic signal from methane-air samples excited at 3.3 μm, Appl. Phys. B 108 (2012) 369–375.
[28] S. Qiao, Y. He, Y. Hu, Y. Ma, Z. Lang, Quartz-enhanced photoacoustic photothermal spectroscopy for trace gas sensing, Opt. Lett. 29 (4) (2021) 5121–5127.
[29] L. Dong, R. Lewicki, K. Liu, P.R. Buerki, M.J. Weida, F.K. Fittel, Ultra-sensitive carbon monoxide detection by using EC-QCL based quartz-enhanced photoacoustic spectroscopy, Appl. Phys. B 107 (2012) 275–283.
[30] R.A. Rooth, A.J.L. Verhage, L.W. Wouters, Photoacoustic measurement of ammonia in the atmosphere influence of water vapor and carbon dioxide, Appl. Opt. 29 (25) (1990) 3643–3653.
[31] F. Wyssocki, A.A. Kosterev, F.K. Tittel, Influence of molecular relaxation dynamics on quartz-enhanced photoacoustic detection of CO_2 at λ=2 μm, Appl. Phys. B 85 (2006) 301–306.
[32] M.A. Moeckli, C. Hilbes, M.W. Sigrist, Photoacosutic multicomponent gas analysis using a Levenberg-Marquardt fitting algorithm, Appl. Phys. B 67 (1998) 449–458.
[33] A. Veres, Z. Bozóki, Á. Mohácsi, M. Szakáll, G. Szabo, External cavity diode laser based photoacoustic detection of CO_2 at 1.43 μm: the effect of molecular relaxation, Appl. Spectrosc. 57 (8) (2003) 900–905.
[34] A. Maity, S. Maithani, M. Pradhan, Cavity ring-down spectroscopy: recent technological advancements, techniques, and applications, Anal. Chem. 93 (1) (2021) 388–416.
[35] S. Maithani, M. Pradhan, Cavity ring-down spectroscopy and its application to environmental, chemical and biomedical system, J. Chem. Sci. 132 (2020) 114.
[36] P. K. Patra, M. Takigawa, K. Ishijima, B.-C. Chol, D. Cunnold, E. J. Dlugokencky, P. Fraser, A. J. Gomez-Pelaez, T. Goo, J. Kim, P. Krummel, R. Langenfelds, F. Meinhardt, H. Mukai, S. O'doherty, R. G. Prinn, P. Simmonds, P. Steele, Y. Tohjima, K. Tsuboi, K. Uhse, R. Weiss, D. Worthy, T. Nakazawa, Growth rate, seasonal, synoptic, diurnal variation and budget of methane in the low atmosphere, J. Meteorol. Soc. Jpn. Ser. II 87 (4) (2009) 636–663.
[37] V. Gros, K. Tsigaridis, B. Bonsang, M. Kanakidou, C. Pio, Factors controlling the diurnal variation of CO above a forested area in southest Europe, Atmos. Environ. 36 (2002) 3127–3135.
[38] J. Wu, D. Guan, F. Yuan, H. Yang, A. Wang, C. Jin, Evolution of atmospheric carbon dioxide concentration at different temporal scales recorded in a tall forest, Atmos. Environ. 61 (2012) 9–14.
[39] Y. Pao, Optoacoustic Spectroscopy and Detection, Academic Press, New York, 1977, pp. 10–25.
[40] W.M. Beltman, Viscothermal wave propagation including acousto-elastic interaction, part I: theory, J. Sound Vib. 227 (1999) 555–586.

Lixian Liu received her B.S. degree of electronic science and technology and doctorate in optical engineering from the University of Electronic Science and Technology of China, in 2012 and 2017, respectively. She is now a full-time associate professor in the School of Physics and Optoelectronic Engineering, Xidian University. Her research field is photoacoustic and optical spectroscopy technologies.

Huiting Huan received his B.S. and Ph.D degrees from the University of Electronic Science and Technology of China in 2012 and 2017, respectively. He is now a researcher and associate professor with the School of Mechano-Electronic Engineering, Xidian University. His main research field includes acoustic, electromagnetic and thermal radiometric non-destructive testing.

Xueshi Zhang is a Ph.D student at the School of Physics and Optoelectronic Engineering, Xidian University. He focuses on the high sensitivity trace gas detection technology.

Le Zhang is a Ph.D. student at the School of Physics and Optoelectronic Engineering, Xidian University. His research interests include photoacoustic spectroscopy and its application to trace gas detection.

Jinsong Zhan received his B.S. and Ph.D degrees from Xidian University of China in 2004 and 2010, respectively. He is now an associate professor with the School of Mechano-Electronic Engineering, Xidian University. His main research field includes weak signal processing and electric circuit designing.

Shaowei Jiang received his B.S. and Ph.D degrees from Zhejiang University and University of Connecticut in 2014 and 2021 respectively. He is now a full-professor at School of Communication Engineering, Hangzhou Dianzi University. He focuses on computational imaging.

Xukun Yin received his Ph.D. degree in atomic and molecular physics from Shanxi University, China, in 2020. From 2018–2019, he studied as a research associate in the electrical and computer engineering department, Rice University, Houston, USA. Currently he is an assistant professor in the School of Physics and Optoelectronic Engineering of Xidian University. His research interests include optical sensors and laser spectroscopy techniques.

Baisong Chen received his Ph.D degree from Rocket Force Engineering University in 2008. He is now a full-time lecturer in the School of Optoelectronic Engineering, Xidian University. His research field is optical spectroscopy and laser detection technologies.

Xiaopeng Shao received his Ph.D degree from Xidian University in 2005. He is a professor at the School of Physics and Optoelectronic Engineering, Xidian University. His research focuses on computational imaging, optical sensing and signal processing.

Xuesen Xu received his B.S. degree in space science and technology from Shandong University in 2013 and doctorate in astronomical technology and methods from the National Astronomical Observatories of the Chinese Academy of Sciences 2018. He is now a full-time associate researcher at the Hangzhou Institute for Advanced Study, University of Chinese Academy of Sciences. His research field is lunar and planetary spectroscopy.

Andreas Mandelis received his B.S. degree in physics from Yale University, New Haven, CT, USA in 1974, followed by M. A., M.S.E., and Ph.D degrees in applied physics and materials science from Princeton University, Princeton, NJ, USA in 1976, 1977 and 1979, respectively. He is a Full Professor of mechanical and industrial engineering; electrical and computer engineering; and the Institute of Biomaterials and Biomedical Engineering, University of Toronto, Toronto, ON, Canada. He is the Director of the Center for Advanced Diffusion-Wave and Photoacoustic Technologies (CADIPT), Toronto. He is an author and coauthor of more than 410 scientific papers in refereed journals and 190 scientific and technical proceedings papers. He is the Editor-in-Chief of the Springer Nature International Journal of Thermophysics, and an Editor of the Journal of Biomedical Optics and the Journal of Applied Physics.